

Inhomogeneous Strain Release during Bending of WS₂ on Flexible Substrates

Martin E. P. Tweedie[†], Yuewen Sheng[†], Syed Ghazi Sarwat[†], Wenshuo Xu[†], Harish

Bhaskaran[†], Jamie H. Warner^{†}*

[†] Department of Materials, University of Oxford, Parks Road, Oxford, OX1 3PH, United
Kingdom

*jamie.warner@materials.ox.ac.uk;

Abstract:

2D materials hold great promise in flexible electronics, but the weak van-der-Waals interlayer bonding may pose a problem during bending, where easy interlayer sliding can occur. Furthermore, thin films of rigid materials are often observed to delaminate from soft substrates during straining. Here we study the influence of substrate strain on some of the heterostructure configurations we expect to find in devices, composed of three common 2D materials: graphene, tungsten disulphide, and boron nitride. We used photoluminescence (PL) spectroscopy to measure changes to the heterostructures with strain applied in situ. All heterostructures were fabricated directly on polymer substrates, using materials synthesised by chemical vapour deposition. We observed an inhomogeneous release of strain in all structures, leading to a non-recoverable broadening of the PL peak and shift of the bandgap. This suggests the need to precondition devices before service to ensure stable behaviour. A gradual time dependent relaxation of strain between strain cycles was characterised using time dependent measurements - an effect which could lead to drift of device behaviour during operation. Further, possible degradation was assessed by performing the strain and relax cycle up to 200

times, where we found little further change after the initial shifts had stabilised. These results have important ramifications for devices fabricated from these and other 2D materials, as they suggest extra processing steps and considerations that must be taken to give consistent and stable properties.

KEYWORDS: 2D materials, heterostructures, sliding, interlayer forces, friction

Introduction:

Since its discovery, graphene has been widely investigated as a material for use in diverse electronics applications,¹ due to its high conductivity,² excellent carrier mobility,³ and monolayer thickness.⁴ However, in recent years attention has turned to other two dimensional (2D) materials that - unlike graphene - have band gaps of a useful magnitude, which is essential for the future implementation of 2D systems in electronics and opto-electronics.⁵⁻⁷ Mechanical exfoliation has enabled a plethora of different 2D materials to be isolated from bulk crystals and many of these are semiconductors with direct bandgaps that span from UV to near IR.⁸⁻¹⁰ One interesting family of semiconducting 2D materials are the transition metal dichalcogenides (TMDs), with many members having direct bandgaps in the visible range in monolayer form.¹¹ Graphene can then be used as a contact to TMDs in devices such as transistors, LEDs, and photodetectors.¹² The final component is a 2D insulator, for which a primary candidate is hexagonal boron nitride (hBN). hBN has an extremely wide bandgap (~ 6 eV)¹³ and so can be used as an insulating layer, gate dielectric, or tunnel barrier.¹⁴

Though it will be difficult for heterostructured devices composed of these materials to compete with the well-established semiconductors such as silicon and III-Vs in established high performance applications,¹⁵ many novel device designs have now been produced with interesting and sometimes unique properties.^{12,16-18} One area in which they compare more favourably is in flexible and/or transparent electronics, with comparable strain resilience^{10,11,15}

and optical transmissivity,^{19,20} and carrier mobilities often far exceeding those of competing technologies such as conducting polymers.¹⁵

The local environment can strongly influence the properties of 2D materials due to their high specific surface area;^{21,22} this typically manifests as changes to the doping level or band gap.^{22–25} For this reason, it is necessary to have an understanding of the interactions between 2D materials in heterostructures. Flexible electronics provide a further complication in the form of strain, which can again cause changes to the bandgap and modify the interactions between the different materials.^{6,26–30} Due to the weak van der Waals out of plane bonding, it is reasonable to expect incomplete transfer of strain from the substrate to the 2D materials.^{29,31–33}

Friction in graphene and other 2D materials is complex and the subject of ongoing research, both by simulation³⁴ as well as using techniques such as atomic force microscopy (AFM)³⁵, and Raman and photoluminescence (PL) spectroscopy.³⁶ Li *et al.*³⁴ used molecular dynamics simulations to model the interaction of a silicon tip with graphene of various layer numbers, showing an increase in friction as layer number decreases due to increased puckering around the probe tip. They further demonstrated that a previously inexplicable transient increase in friction force over the first few atomic periods results from the formation of progressively deepening traps at the interface, where out-of-plane deformation increases the quality of frictional contact. The materials boundary condition is also important, where a loose and wrinkled sheet shows much higher friction than a tight and smooth one. This will have relevance to 2D electronics, with devices composed from stacks of different 2D materials of differing geometries, and demonstrates the importance of out of plane deformations. Liu *et al.*³⁶ used Raman and PL mapping to study the distribution of strain within triangular domains of monolayer MoS₂ on strained PDMS substrates, finding that at higher strains, only ~10 % of strain is transferred, and that transferred strain propagates through the triangle beginning at the point aligned most closely with the strain axis. Though incomplete strain transfer has

previously been observed in 2D materials on soft substrates under tension, there is significant scope for improvement in the description of the mechanism and its influence on different heterostructures.

To understand the influence these effects may have in vertically stacked 2D layered systems of different materials, herein we study the changes to the PL spectra of the direct bandgap TMD tungsten disulphide (WS_2) in several different heterostructure configurations involving graphene and hBN, in response to strain. Polyethylene naphthalate (PEN), a material commonly employed in flexible electronics, was used as the substrate due to its high chemical, thermal, and hydrolytic resistance.³⁷ The chosen heterostructures were (stacked vertically from top to bottom): WS_2/PEN , $\text{WS}_2/\text{hBN}/\text{PEN}$, $\text{WS}_2/\text{Graphene}/\text{PEN}$, and $\text{WS}_2/\text{hBN}/\text{Graphene}/\text{PEN}$, representing two possible device channels, contacts, and gated channels respectively. Chemical vapour deposition (CVD) was used to grow the 2D materials, to demonstrate the reproducibility of these findings and their applicability to materials suitable for large scale manufacturing.

Results & Discussion

All materials were grown *via* CVD using previously reported methods, producing large domains of WS_2 (Fig. 1a), and continuous films of typically bilayer graphene and hBN (Fig. 1b,c), with the quality and coverage determined by optical microscopy and SEM. Raman spectroscopy was used to characterise the films and determine the layer number (Fig. 1d-f). Details of the growth processes are available in the Methods. We used the well-established wet chemical etching technique to remove the growth substrate, with transfer predominantly achieved using wet/aqueous transfer (aq.). This was compared with our previously reported non-aqueous transfer technique (non-aq.) in which isopropyl alcohol is used to displace water, as this can modulate interlayer interactions by reducing trapped interfacial contamination.¹⁶

Further information is provided in the Methods, and schematics of the two processes are shown in Fig. S1. The heterostructures were stacked layer-by-layer from 1x1 cm films of graphene and hBN, and domains of WS₂ typically 100-200 μm in size.

PL measurements were performed on the different heterostructures (shown schematically in Fig. 1g) before, during and after the application and relaxation of strain by bending. The maximum strain was 2.5 %, which was deemed to easily accommodate the maximum strain that real devices will experience.³⁸ The strain was then relaxed and the cycle repeated a further 2-3 times, after which point the PL changes were observed to stabilise.

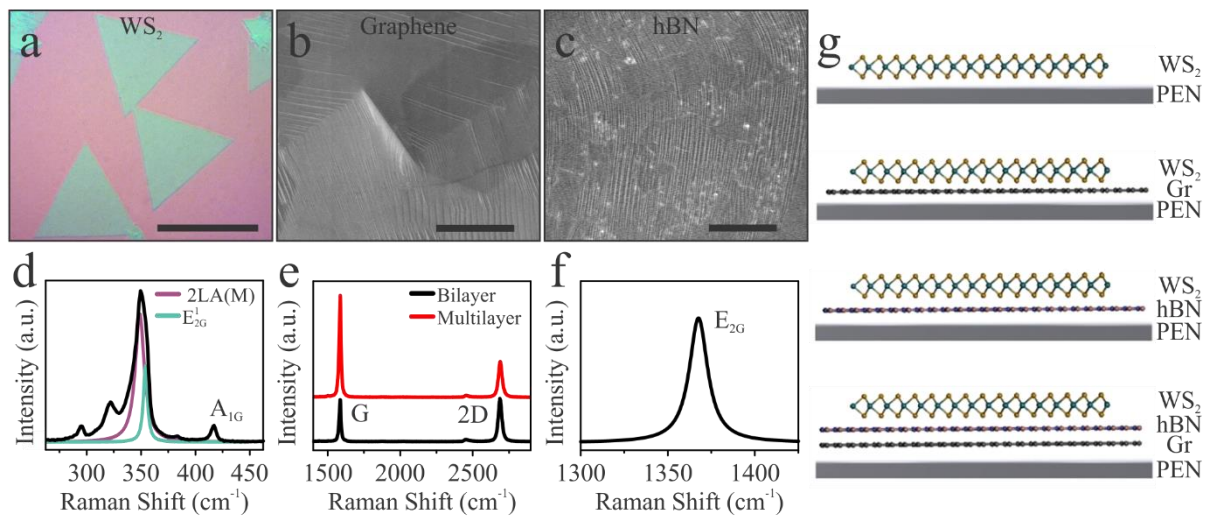


Fig. 1: Characterisation of the studied 2D materials and schematics of their configurations in heterostructures. (a) Optical (200 μm scale bar) and (b,c) SEM (5 μm scale bar) images of WS₂, graphene, and boron nitride, respectively. See Fig. S2 for further images of typical WS₂ domains before and after transfer. (d-f) Raman spectra from the same, showing: (d) the combined 2LA(M)/E_{2G}¹ (second order LA/in-plane, individual contributions revealed by Lorentzian fitting, other peaks omitted) and A_{1G} (out of plane);³⁹ (e) the G (sp² specific) and 2D (second order, specific to graphitic materials);⁴⁰ (f) and the E_{2G} (sp² specific, analogous to G peak in graphene)⁴¹ characteristic Raman modes, respectively. The ratio of peak intensities indicates that WS₂ is monolayer (d) and that graphene is bilayer with small multilayer islands (e), and the position of the peak indicates that the hBN in (f) is bilayer. (g) Schematic illustrations showing the layer ordering of the four heterostructures.

All measurements were carried out using a spectrometer and 532 nm laser, with strain applied in situ by collapsing radius test using a custom-built holder (Fig. S3). The strain in the substrate surface was calculated using equation [1]:

$$\varepsilon = \frac{t \sin \theta}{d} \quad [1]$$

outlined by McCreary *et al.*⁴² and others.^{29,43–45} Here ε is the strain, θ is the angle of the tangent of the substrate at the point of contact, d is the plate separation of the holder, and t is the substrate thickness. The thickness of the 2D materials can be neglected as it is at least 5 orders of magnitude less than the substrate (~ 0.8 nm for bilayer graphene⁵ and hBN⁴¹ and 0.6 nm for WS₂⁴⁸). Due to the convex shape of the substrate as strain is applied, it was only possible to measure the central region of the specimen under tension, so the number of measurable WS₂ domains was optimised by mapping the growth substrate to determine the area with the best coverage of high quality domains and aligning it with the centre of the substrate (Fig. S1b). This had the advantage of confining our measurements to a region of approximately uniform strain. For all PL measurements, we kept the laser power constant at 1.1 mW or ~ 4 kW/cm², which was sufficient to provide an adequate signal-to-noise ratio without inducing significant thermal effects.^{46,47}

The PL spectrum of WS₂ comprises two component emissions arising from the recombination of: excitons (A); and trions (A⁻), quasiparticles composed of an exciton bound to a hole or in this case an electron due to the intrinsic n-type doping of CVD-grown WS₂.^{48–50} Emission from the latter leads to broadening of the PL spectrum on the low energy side. Properties that can typically be drawn from these include the bandgap of the material, the level of doping, and the trion binding energy.^{48–50} However, other mechanisms can change the peak shape and hamper the interpretation of these properties, so we have focussed on the mechanical interfacial interactions between the WS₂ and underlying materials and the substrate. Fig. 2(a)

shows the broadening of the peak that occurs after transfer from the growth substrate, likely caused by the higher substrate roughness causing uneven strain distributions; the further broadening and redshift occurs due to straining. Fig. 2b-d shows the general response of the fitted A & A- emissions to strain cycling.

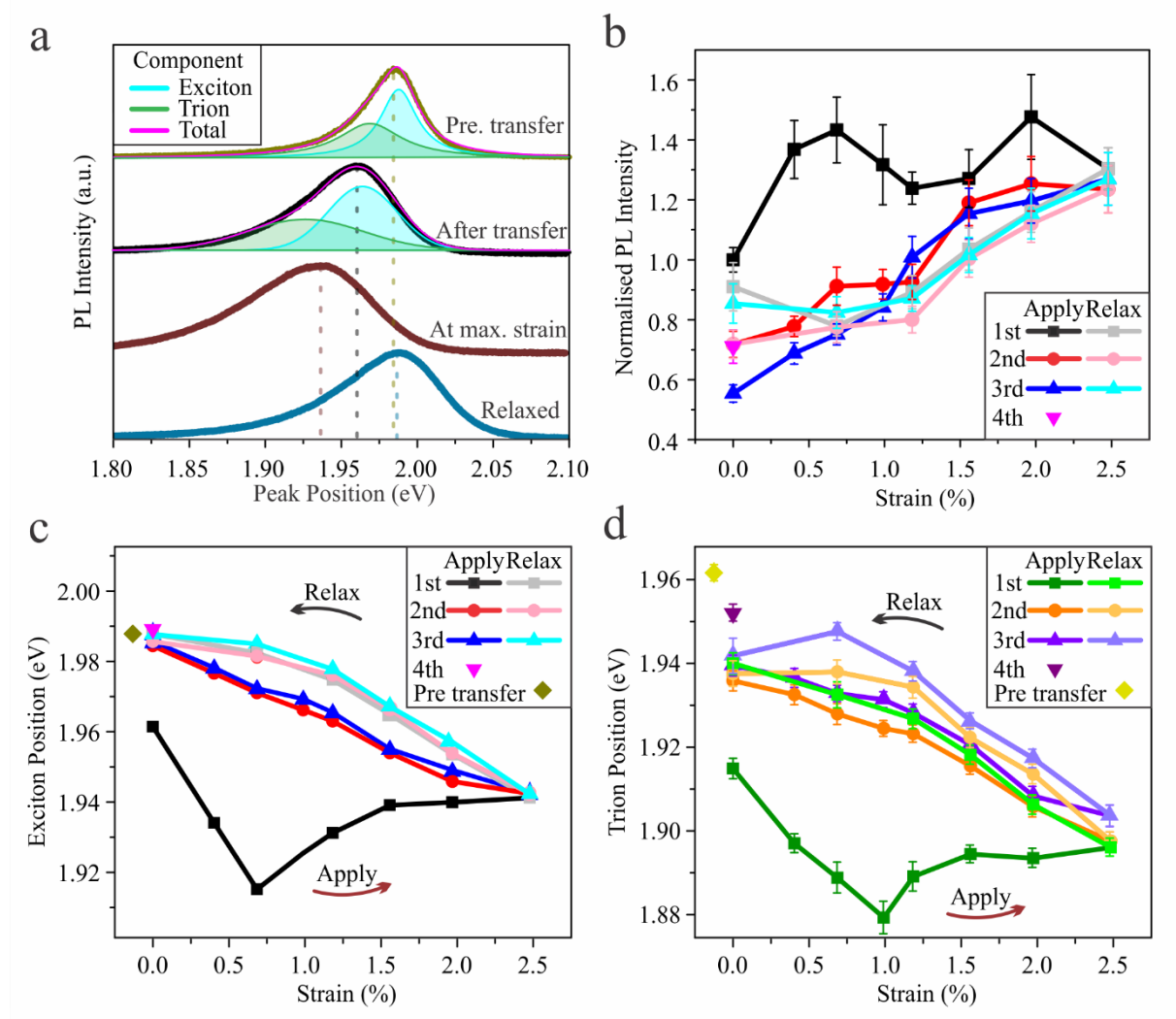


Fig. 2: Example spectra and analysis of one of the studied heterostructures. (a) PL spectra of WS₂ taken before and after transfer, at maximum strain, and after strain was relaxed for the WS₂/Graphene/PEN aq. heterostructure. Note that Lorentzian fits were used to extract information about the exciton and trion peaks on the pre-transfer spectrum, while due to broadening Gaussian fits were used post-transfer. (b) Changes to total emission intensity across 3 strain cycles in the WS₂/Graphene/PEN non-aq. heterostructure as strain is applied and relaxed, and a 4th measurement at 0 % strain. Changes to (c)

exciton (A) and (d) trion (A-) positions for same. Pre-transfer values and standard errors are also indicated. Note stabilisation to a hysteresis loop after the 1st application of strain for both A and A- peaks.

During the first strain cycle, an unexpected broadening and distortion of the peak shape occurs in all (>100) domains measured (Fig. 3a), leading to incorrect fitting of both the exciton and trion peaks, observable as a pronounced discontinuity in the fitted peak shapes (see Fig. S4a-c for more details). This causes the increase in the standard error of the peak intensity and trion position (Fig. 2b-d). Our reasoning for the evolution of the peak shape is as follows: After transfer the peak is redshifted by a combination of an induced tensile strain in the layers arising from thermal mismatch and conformation of the sheet to the rough PEN surface, and the lower relative permittivity of the PEN substrate compared to the SiO_2 that the WS_2 was grown on increasing the binding energy of the excitons and so lowering the energy released during recombination.^{37,51} When strain is applied, there is initially complete uptake of the applied strain by the WS_2 . Once a threshold of $\sim 0.7\%$ strain is passed, there is partial debonding and loss of coherency between the 2D materials and underlying substrate that leads to broadening of the PL peak. Once the strain is relaxed, there is a lingering blueshift relative to the initial position that is only partially recovered, caused by the debonding of the layers releasing the built in tensile strain described above. With this strain released, when the substrate is relaxed the tensile strain in the WS_2 is less than before strain was applied, leading to the observed shift to the peak position. This process is outlined schematically in Fig. 3b.

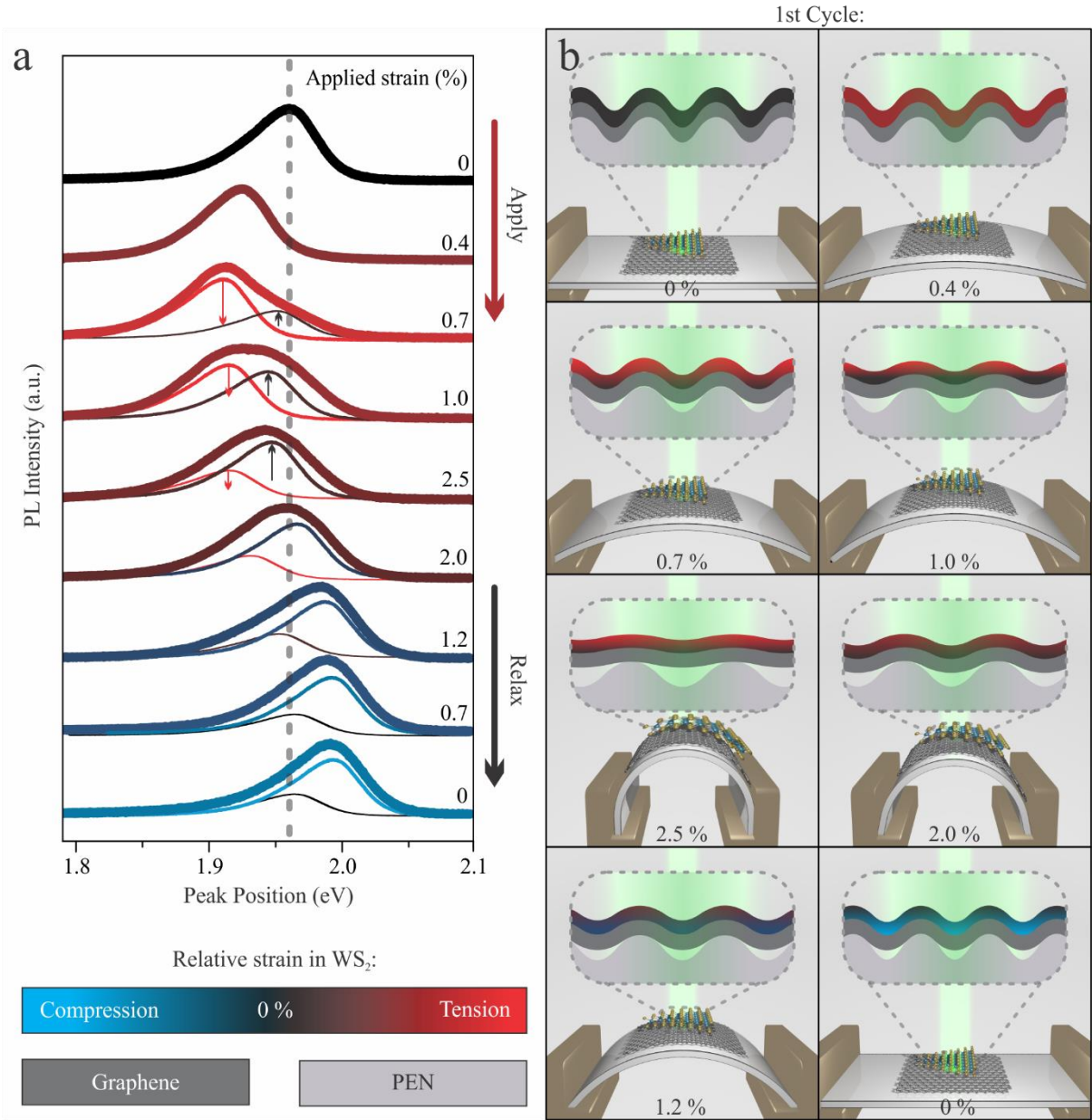


Fig. 3: Details of the debonding process that takes place during the first strain cycle. (a) Example peak shapes (taken from the first strain cycle of the WS₂/Graphene/PEN aq. heterostructure) are shown normalised by intensity as strain is applied and relaxed, with approximate contributions from bonded (more tensile) and debonded (less tensile) regions indicated. (b) Schematics showing the debonding and loss of coherency between the WS₂ and underlying material in the first strain cycle, with exaggerated height profile indicating surface roughness inset. Colour indicates approximate strain, with 0 % set at the initial peak position. This shows the evolution of the peak shape, starting with a redshift while there is full coherency with the substrate, followed by partial loss of coherency at higher strains and so an apparent broadening and blueshift. At the maximum strain, the original peak shape is practically

recovered, indicating that strain is mostly homogeneous. Intensity changes are consistent with changes shown in Fig. 4c.

The general form of the changes to the spectrum is shown in Fig. 3a for the application and relaxation of substrate strain. Intensity changes are omitted for clarity, but follow the same trends shown in Fig. 4c. The strain in the WS₂ initially increases monotonically with the substrate, leading to a well-documented red-shift common to TMDs due to the reduction in the bandgap.^{27,52–54} At strains of 0.4–1 %, there is a transition where sliding and debonding between the 2D materials and underlying substrate starts to occur, a transition we recently also observed in a Kelvin probe microscopy (KPM) study of the WS₂/Graphene/PEN heterostructure.⁵⁵

This general behaviour was common to the 4 heterostructure configurations tested: a pronounced change in the peak shape resulting from partial debonding of the 2D materials perpendicular to the strain axis, beginning in the roughness valleys of the substrate, leading to an inhomogeneous distribution of strain and so emission from a distribution of bandgaps (Fig. S4d). This process is similar to predictions in the ideal case by Kumar *et al*³¹, as well as the observations by Susarla *et al*⁵⁶ in synthesised WS₂/MoS₂ heterostructures, with our transition occurring at lower strains than the latter due to weaker interlayer coupling resulting from more interfacial contamination in our manually stacked structures.

As further strain is applied, the relative area that is debonded rapidly increases, owing to the unique ease of out of plane distortion in 2D materials. This leads to a decreased contribution from the redshifted component and so an overall blueshift to the peak position. With the roughness features occurring over length scales that are smaller than the laser spot size of ~6 μm we effectively sample a distribution of strains over bonded and debonded regions. See Fig. S5 for AFM profiles of the surface of the WS₂/Gr/PEN aq. heterostructure before and after the application of strain. We hoped to use AFM to image the debonding as a reduction in surface

roughness but were unable to resolve any difference. This again is likely due to the ease of out of plane distortions,³⁵ and the limited resolution because of the surface roughness.

By 2.5 % strain the emission is dominated by the debonded regions and the initial peak shape is mostly recovered, with a smaller redshift due to the partial strain transfer. The transition can be best observed with reference to the changes to the global peak position (Fig. 4a) and FWHM (Fig. 4b), where there is a marked change above 0.4 % strain, with a partial reversal of the initially strong redshift, and a broadening of the PL peak width. The cause of the increase in standard error at the onset of coherency loss is the inherently random nature of the debonding leading to different domains losing coherency at different rates. We believe that the debonding is primarily between the substrate and first layer of 2D materials, but cannot rule out debonding between layers of 2D materials.

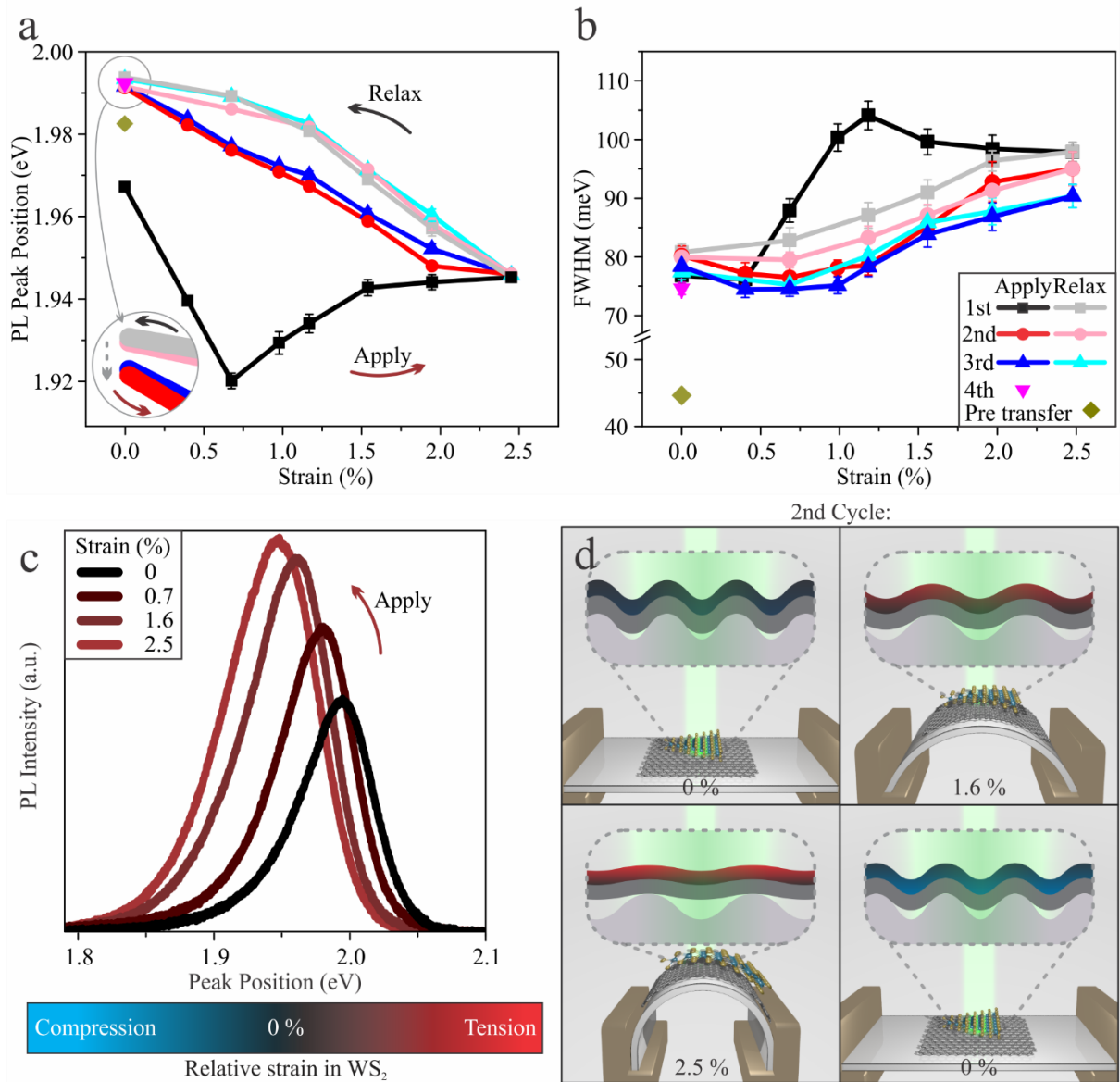


Fig. 4: Changes to peak position and shape, and details of the stabilised strain behaviour in subsequent strain cycles after debonding. (a) Overall peak position and (b) FWHM for WS_2 /Graphene/PEN non-aq. heterostructure over 3 strain cycles, and before transfer. Pre-transfer values and standard errors are also indicated. The inset in (a) shows the small relaxation/blueshift that occurs between strain cycles. (c) Changes to peak position and intensity as strain is applied. Note no major changes to peak shape over full range of strain, indicating that a stable state has been reached. (d) Schematics showing the effect of strain on the WS_2 in the second strain cycle as a result of the debonding in the first cycle, with

exaggerated height profile inset. Colour indicates approximate strain, with 0 % set at the initial peak position.

Fig. 4c shows the changes to the emission during the second strain cycle. As the WS₂ has largely debonded from the underlying materials, the degree of strain transfer and so the magnitude of the redshift is smaller, and the strain distribution is largely homogeneous, as reflected in the more modest broadening. Two mechanisms contribute to the associated increase in luminescence intensity. Firstly, an increase in the absorbance cross section as the bandgap narrows leads to more of the incident light being absorbed. Secondly, due to the increasingly large offset between the K (direct, radiative) and the Σ (indirect, non-radiative) conduction band minima as strain increases, there is a reduction in the quenching caused by the drain of carriers from K to Σ ; this draining occurs since the Σ minima is lowered in energy due to bandgap renormalisation caused by the high density of optically generated excitons.⁵⁷ We believe that the expected quenching at higher strains is not observed due to the incomplete strain transfer, though if some parts of the WS₂ are above the expected threshold where the intensity begins to decrease again while others are below, this would explain the relatively modest PL intensity enhancement we observe compared to that predicted by Steinhoff *et al.* for MoS₂.⁵⁷

Further strain cycling reveals stabilisation to a hysteresis loop, in which the debonding and interfacial sliding lead to incomplete strain transfer (Fig. 4a). This contrasts the findings of Liu *et al.*³⁶, who observed no hysteresis in their measurements of strained MoS₂ on PDMS, though they observed similarly incomplete strain transfer. The origin of this behaviour is that when the substrate is initially relaxed, the WS₂ is placed in compression, due to the partial relaxation of tensile strain in the WS₂ following the debonding during the application of strain. Over time, this compressive strain relaxes and the heterostructure partially re-conforms with

the substrate, leading to the small redshift highlighted in the inset of Fig. 4a. When the substrate is subsequently strained again, initial uptake of the strain is lower than in the first strain cycle and decreases further at higher strains. The reverse is true as the strain is relaxed, initially blueshifting the spectrum more rapidly before levelling off as substrate strain approaches zero.

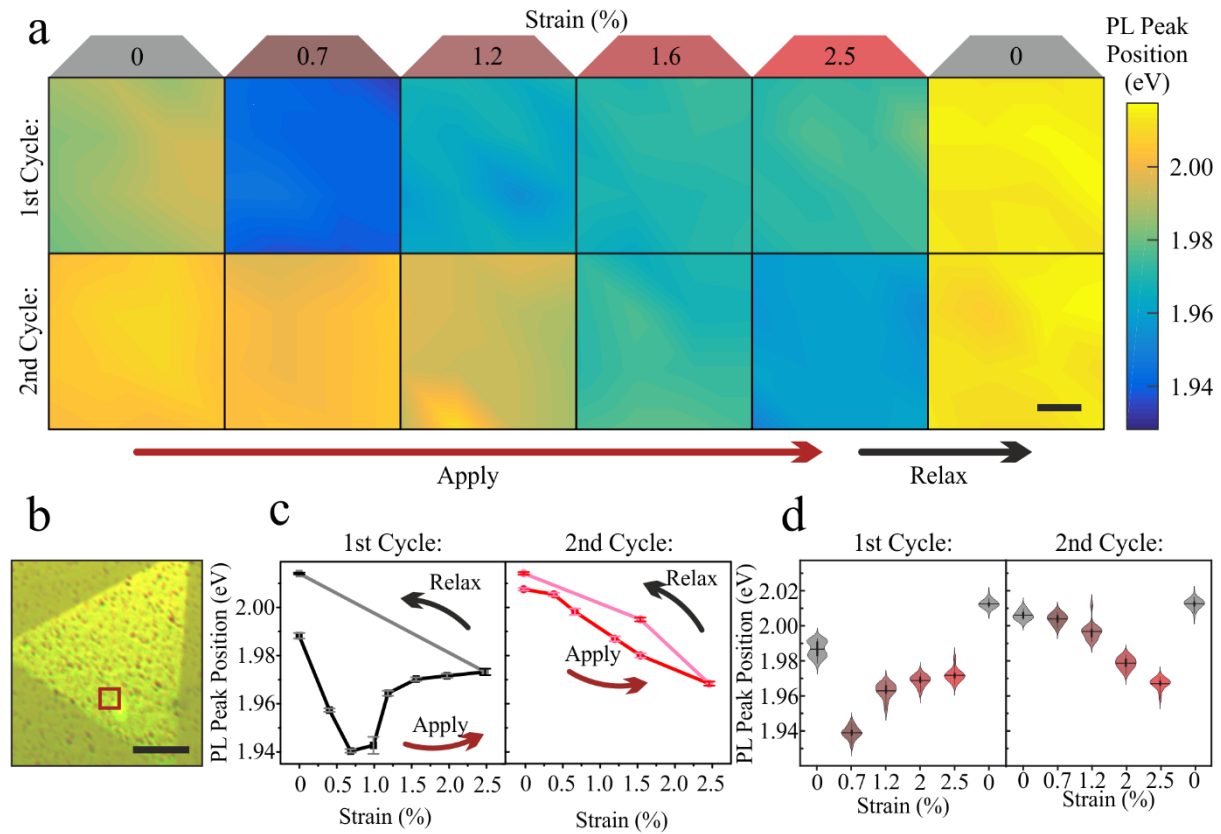


Fig 5: Local mapping of the peak shifts during the first strain cycle on the WS₂/Graphene/PEN non-aq. heterostructure. (a) Maps of PL peak positions during the first and second cycle, as strain is applied and relaxed. Scale indicated in the last frame is 2 μm. (b) False colour micrograph with mapping area indicated and a 20 μm scale bar. (c) Average peak positions at each strain position for the first and second cycle, and (d) violin plots showing the distribution of peak positions within the mapped area. Note large scale shift and release during first strain cycle and comparatively small shifts during second cycle, accompanied by a reduction in the spread of the data in the second cycle.

To validate the debonding mechanism, we conducted local mapping of the peak positions during the same strain cycling described above on the WS₂/Graphene/Pen non-aq.

heterostructure and compared this to mapping of the same heterostructure with a 50 ± 5 nm poly(methyl methacrylate) (PMMA) coating applied to the PEN surface to modify the surface roughness. The roughness of the PEN and PMMA/PEN substrates was characterised by AFM (Fig. S6a-c), and found to be $R_a = 6.89 \pm 1$ nm for PEN and $R_a = 9.49 \pm 1$ nm for PMMA/PEN. The PMMA film thickness was measured by cross-sectional SEM (Fig. S6d). In the first strain cycle, we observed small variations over the area we examined for the structure without PMMA (Fig. 5a) and larger variations in the structure with PMMA (Fig. S7 a), in accordance with the increase in roughness. The later and broader onset of debonding in the PMMA structure is caused by the lower degree of strain transfer from the substrate through the softer PMMA layer (Fig. S7c). This is also the reason for the observed smaller total peak shift in this structure. After debonding has taken place, the effect of the differing roughness values is reduced, and the behaviour is similar, accompanied by a reduction in the spread of the peak positions in both cases (Fig. 5d & S7d).

Little difference was observed in the response of the different heterostructures, and in all cases the same debonding and coherency loss occurs. The key changes are summarised in a bar chart in Fig. 6. Small variations up to ~ 10 meV were found between the peak positions pre-transfer, attributed to compositional changes and differing amounts of post growth strain. Random variations in the surface contact also lead to different magnitudes of observed shift post transfer, after release of the inbuilt strain, and over each strain cycle. Based on the value calculated by Li *et al.* for bandgap shifts per cent strain (0.19 eV/ %),⁵⁸ the magnitude of strain transfer never exceeds ~ 0.45 %, which is less than a fifth of the applied substrate strain. This again contrasts the findings of Liu *et al.*³⁶, who found that for MoS₂, the strain transfer was low for low modulus substrates, but increased dramatically for higher modulus substrates such as PEN.

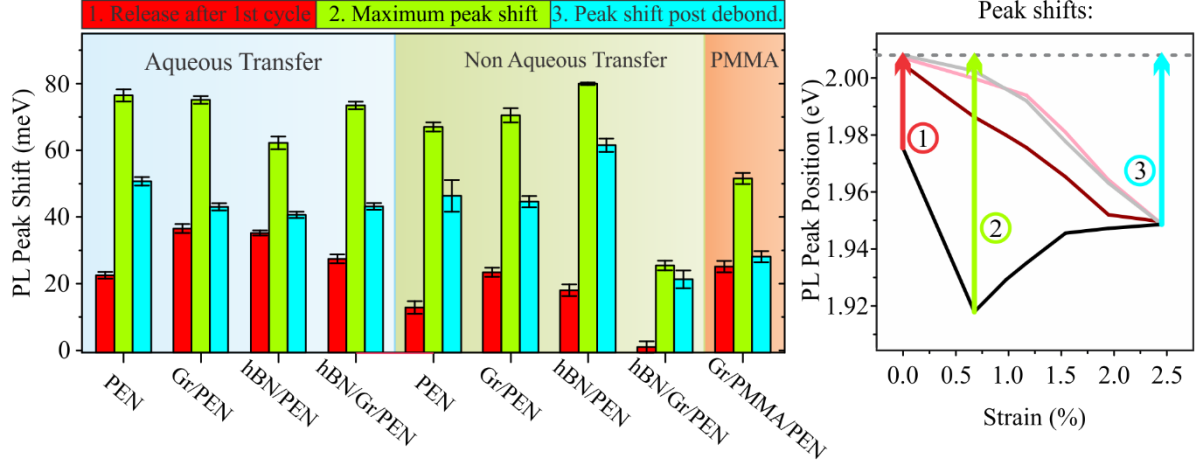


Fig. 6: Summary of the key changes to the peak position during straining, for all heterostructures transferred by both aqueous and non-aqueous methods, as well as the WS₂/Graphene/PMMA/PEN heterostructure. This illustrates the similarities in the responses of all heterostructures, in terms of the: amount of strain released after the 1st strain cycle, maximum change between the unstrained position and at the point of coherency loss, and total changes between 0 % and 2.5 % strain for the 2nd strain cycle, i.e. after debonding. These peak shifts are detailed in a simplified plot of peak position as a function of strain.

To study the time dependent redshift that occurs between measurements, we chose the WS₂/hBN/PEN heterostructure as an example in an attempt to control for possible other influences on the properties from electronic effects, as hBN has been shown to behave as an excellent screening layer when used as a substrate for other 2D materials.^{59,60} PL measurements were performed over the course of several hours at regular intervals, after holding the substrate at 2.5 % strain then returning to zero. This confirmed that a residual blueshift remains after the substrate strain is relaxed. As described above, the blueshift following the first strain cycle can only be partially recovered following removal of the substrate strain, due to the release of the

built in tensile strain arising from the transfer process (Fig. 7a). After the second strain cycle, the magnitude of blue shift is significantly smaller (Fig. 7b).

By annealing the structure at the glass transition temperature of the substrate (PEN $T_g = 120\text{ }^\circ\text{C}$), we found that the emission was blue shifted, and the peak slightly sharpened (Fig. 7c,d). This can be explained by an increase in the coherency between the substrate and the WS₂, leading to a slight compressive strain as the debonded regions flatten out. The sharpening of the peak is caused by an increase in the homogeneity of the strain, and was stable over the time measured.

To demonstrate the resilience of these structures, after annealing we repeated the strain cycling up to 200 times, measuring the PL response at several intervals. This shows the stability of the response, in terms of the peak position – barring strain relaxation effects – as well as the FWHM and PL intensity (Fig. 7e-g). To ensure consistency between measurements, all measurements were taken one hour after the strain cycling was performed, limiting the influence of the previously described relaxation mechanism. This provides additional evidence for the fact that the strain transfer reaches a stable state following the initial strain cycle, where the strain is no longer high enough to produce any more slippage so the peak position at 0 % strain does not change further. The reason for the observed broadening of the peak is the increased inhomogeneity of the strain following the cycling as compared to immediately after

annealing.

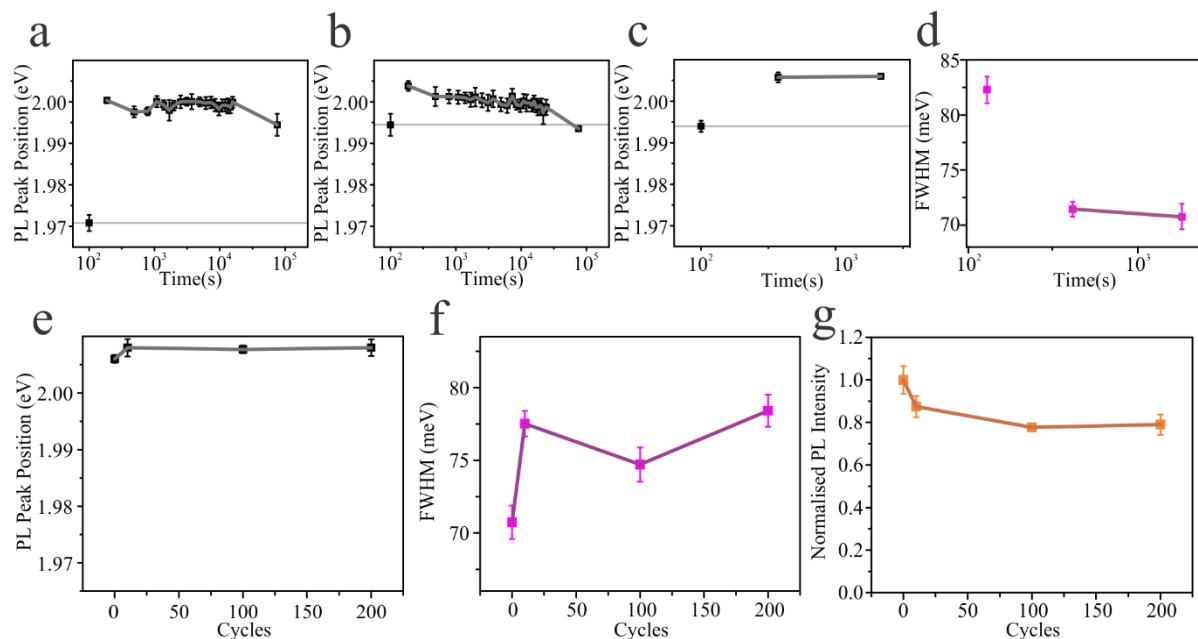


Fig. 7: Changes to the PL peak over time before and after annealing, and as result of repeated strain cycles. Positions following strain cycling for the (a) 1st and (b) 2nd time, and (c) after annealing and straining for the 1st time. (d) The reduction in FWHM after annealing. The isolated points show the position immediately before the application of strain, with horizontal lines plotted as a guide to the eye. (e) Peak position taken 1 hour after cycling strain up to 200 times, and the corresponding (f) FWHM and (g) normalised intensity. All peak position plots are displayed over the same energy range for ease of comparison.

Conclusions

In summary, we have demonstrated a mechanism by which the expected incomplete strain transfer to 2D materials on flexible PEN substrates takes place, largely independent of the different heterostructure configurations and fabrication techniques used. These findings serve to illustrate that for 2D heterostructures to be used in flexible electronics, careful control of the processing will be required in order to avoid the unstable behaviour we have observed to varying degrees across all of the different structures studied. Since the debonding transition occurs within what we consider to be the useful operating strain range, this suggests the need

for extra processing steps to release the built in tensile strain arising from the fabrication process to produce stable and consistent behaviour across multiple devices. However, the demonstration of stable behaviour following the initial debonding is encouraging, as this indicates that after an initial ‘preconditioning’ strain cycle, the properties of the heterostructures are consistent and as such would be suitable for service.

Methods

CVD Synthesis All 2D materials were grown by CVD. The details of each process are as follows:

Graphene A piece of 25 μm thick copper foil (99.8 % purity, Alfa Aesar) was cleaned by sonication in acetone and isopropyl alcohol (IPA) for 10 minutes each. CVD was performed using parameters based on our previous work, at atmospheric pressure. The system was first purged with a mixture of H_2 and Ar (BOC) for 30 minutes, before ramping up the furnace temperature to 1060 $^{\circ}\text{C}$ at a rate of 60 $^{\circ}\text{C min}^{-1}$. After annealing at this temperature for 1 hour, graphene growth was achieved by introducing CH_4 (1 % in Ar, BOC) to the system and holding at 1060 $^{\circ}\text{C}$ under a mixed atmosphere of Ar, H_2 and CH_4 (4 % H_2 , 0.01 % CH_4) for a further hour. Following growth, the CH_4 was switched off and the graphene covered foil was fast cooled under an atmosphere of argon and hydrogen by moving the furnace away from the substrate.

Boron Nitride A piece of 25 μm thick copper foil (99.8 % purity, Alfa Aesar) was cleaned of oxide by sonication in 1M HCl for 10 minutes, followed by sonication in deionised (DI) water, acetone and IPA for ten minutes each. Ammonia borane was used as the source for borazine gas, and was placed in a separate heated chamber upstream of the main furnace. The system was first purged with Ar, before isolating the precursor chamber and purging the main tube with a mixture of Ar and H_2 (3.75 % H_2). The furnace was then ramped up to 1000 $^{\circ}\text{C}$ at a rate of 60 $^{\circ}\text{C min}^{-1}$ and held at this temperature for 1 hour to anneal the substrates. The concentration of hydrogen was then increased to 25 % and the gas flow rate reduced while the ammonia borane was heated up to ~ 120 $^{\circ}\text{C}$ and the main furnace temperature increased to 1040 $^{\circ}\text{C}$. The evolved gas was then introduced to the reactor and growth allowed to proceed for 25 mins. Once growth was complete, the gas feed was set back to 3.75

% hydrogen at the higher flow rate, and fast cooling was achieved by moving the furnace away from the substrate.

WS₂ Monolayer WS₂ was synthesised by two-zone vapour transport under an argon atmosphere, at atmospheric pressure using parameters based on our previous work.⁶¹ A silicon chip with 300 nm oxide (University Wafer) was cleaned by sonication first in DI water, then acetone and IPA for 15 minutes each. Further cleaning was performed by oxygen plasma at 90 W for 15 minutes. Sulphur powder (>99.5 % purum grade, Sigma Aldrich) was placed directly in the furnace tube and centred in furnace 1. WO₃ powder (>99.9 % puriss. grade, Sigma Aldrich) was placed directly in a narrower tube that was placed inside the main furnace tube and aligned with the centre of furnace 2, downstream of the sulphur. This acts to keep the evaporated sulphur vapour from coming into contact with the WO₃ powder, instead reacting with it when adsorbed on the substrate surface. The silicon substrate was placed downstream of the two precursors, adjacent to the inner tube but still within furnace 2. After purging the system with argon, growth was initiated by first ramping furnace 2 to 470 °C at a rate of 40 °C min⁻¹, then ramping furnace 1 to 183 °C at a rate of 30 °C min⁻¹ while increasing furnace 2 to 1150 °C at the same rate as before. The system was then held at this temperature for ~5 minutes while growth occurred, before lowering the Ar flow to prevent delivery of further precursor. Excess sulphur was purged by heating furnace 1 to 400 °C and increasing the Ar flow rate again, once furnace 2 was sufficiently cool to prevent further reactions. Fast cooling was then achieved by moving both furnaces away from the substrate.

Transfer of 2D materials Transfer of all materials was achieved by the well-established wet chemical etching technique. First, a PMMA (A8 495K, Microposit) scaffold was spincoated onto the surface at 4500 rpm. After baking at 180 °C for 90 seconds, the substrate was floated on the surface of an etchant solution (SiO₂/Si wafer: 1M KOH, Sigma Aldrich; Cu foil: 0.2 M (NH₄)₂S₂O₄, Sigma Aldrich) for ~3 hours, until the substrate was detached (SiO₂/Si wafer) or dissolved (Cu foil). The floating films were then washed several times in DI water before being transferred to the target substrate (250 µm polyethylene naphthalate film, Teonex Q51, Teijin-Dupont). This was accomplished in one of two ways: manually scooping the film directly from the DI water onto the substrate, or using a non-

aqueous technique described in our previous work. This non-aqueous technique involves sliding the film into place using IPA as a carrier, removing excess water in the process. Both procedures are shown schematically in the supplementary information (Fig. S1). Following transfer, the procedure was identical for both techniques: proper adhesion was ensured by baking the substrate at 120 °C for 25 minutes, and removal of the PMMA accomplished by immersion in acetone at 45 °C for at least 3 hours. For transfer to PMMA, photoresist (maN 1420, Microposit) was used as the scaffold. This was removed using IPA.

Photoluminescence Spectroscopy A diode-pumped 532 nm solid-state laser (DJ532-40, Thorlabs) was reflected by a dichroic beam splitter and focussed to a spot of ~6 µm diameter by a 10× objective lens. Spectra were collected by a custom-built confocal microscope coupled to a spectrometer (Acton SP-2300 spectrometer with PIXIS 100 CCD detector, Princeton Instruments).

Acknowledgements

M.T. thanks the EPSRC for supporting this research (EP/M50659X/1). Y.S. acknowledges support from the Armourers & Brasiers Gauntlet Trust, Great Britain–China Educational Trust and St. Cross College, Oxford. S.G.S. and H.B. acknowledge support from EPSRC via the Manufacturing Fellowship EP/J018694/1 as well as the WAFT collaboration (EP/M015173/1). S.G.S. acknowledges a Felix Scholarship that supports his DPhil. W.X. acknowledges support from The Queen’s College, Oxford. J.H.W. thanks the Royal Society and the ERC Consolidator grant.

Supporting information

Supporting Information Available: A description of the PL spectra processing, schematics of the transfer process, false colour optical micrographs of the WS₂ domains before and after transfer, diagrams of the strain holder setup, a typical AFM line profile of the PEN substrate, characterisation of the roughness of the PEN substrate without and with PMMA coating, and the mapping characterisation of the WS₂/Gr/PMMA/PEN aq. heterostructure. This material is available free of charge online at the ACS website via the Internet at <http://pubs.acs.org>.

References

- (1) Jariwala, D.; Sangwan, V. K.; Lauhon, L. J.; Marks, T. J.; Hersam, M. C. Carbon Nanomaterials for Electronics, Optoelectronics, Photovoltaics, and Sensing. *Chem. Soc. Rev.* **2013**, *42*, 2824–2860.
- (2) Geim, A. K. Graphene: Status and Prospects. *Science* **2009**, *324*, 1530–1534.
- (3) Novoselov, K. S.; Geim, A. K.; Morozov, S. V.; Jiang, D.; Zhang, Y.; Dubonos, S. V.; Grigorieva, I. V.; Firsov, A. A. Electric Field Effect in Atomically Thin Carbon Films. *Science* **2004**, *306*, 666–669.
- (4) Schwierz, F.; Granzner, R.; Pezoldt, J. Two-Dimensional Materials and Their Prospects in Transistor Electronics. *Nanoscale* **2015**, *7*, 8261–8283.
- (5) Ohta, T.; Bostwick, A.; Seyller, T.; Horn, K.; Rotenberg, E. Controlling the Electronic Structure of Bilayer Graphene. *Science* **2006**, *313*, 951–954.
- (6) Ni, Z. H.; Yu, T.; Lu, Y. H.; Wang, Y. Y.; Feng, Y. P.; Shen, Z. X. Uniaxial Strain on Graphene: Raman Spectroscopy Study and Band-Gap Opening. *ACS Nano* **2008**, *2*, 2301–2305.
- (7) Han, M. Y.; Özyilmaz, B.; Zhang, Y.; Kim, P. Energy Band-Gap Engineering of Graphene Nanoribbons. *Phys. Rev. Lett.* **2007**, *98*, 206805.
- (8) Bhimanapati, G. R.; Lin, Z.; Meunier, V.; Jung, Y.; Cha, J.; Das, S.; Xiao, D.; Son, Y.; Strano, M. S.; Cooper, V. R.; Liang, L.; Louie, S. G.; Ringe, E.; Zhou, W.; Kim, S. S.; Naik, R. R.; Sumpter, B. G.; Terrones, H.; Xia, F.; Wang, Y.; Zhu, J.; Akinwande, D.; Alem, N.; Schuller, J. A.; Schaak, R. E.; Terrones, M.; Robinson, J. A. Recent Advances in Two-Dimensional Materials beyond Graphene. *ACS Nano* **2015**, *9*, 11509–11539.
- (9) Butler, S. Z.; Hollen, S. M.; Cao, L.; Cui, Y.; Gupta, J. a.; Gutiérrez, H. R.; Heinz, T. F.; Hong, S. S.; Huang, J.; Ismach, A. F.; Johnston-Halperin, E.; Kuno, M.; Plashnitsa, V. V.; Robinson, R. D.; Ruoff, R. S.; Salahuddin, S.; Shan, J.; Shi, L.; Spencer, M. G.; Terrones, M.;

- Windl, W.; Goldberger, J. E. Progress, Challenges, and Opportunities in Two-Dimensional Materials beyond Graphene. *ACS Nano* **2013**, *7*, 2898–2926.
- (10) Wang, Q. H.; Kalantar-Zadeh, K.; Kis, A.; Coleman, J. N.; Strano, M. S. Electronics and Optoelectronics of Two-Dimensional Transition Metal Dichalcogenides. *Nat. Nanotechnol.* **2012**, *7*, 699–712.
- (11) Jariwala, D.; Sangwan, V. K.; Lauhon, L. J.; Marks, T. J.; Hersam, M. C. Emerging Device Applications for Semiconducting Two-Dimensional Transition Metal Dichalcogenides. *ACS Nano* **2014**, *8*, 1102–1120.
- (12) Mak, K. F.; Shan, J. Photonics and Optoelectronics of 2D Semiconductor Transition Metal Dichalcogenides. *Nat. Photonics* **2016**, *10*, 216–226.
- (13) Wang, X.; Hooper, T. N.; Kumar, A.; Priest, I. K.; Sheng, Y.; Samuels, T. O. M.; Wang, S.; Robertson, A. W.; Pacios, M.; Bhaskaran, H.; Weller, A. S.; Warner, J. H. Oligomeric Aminoborane Precursors for the Chemical Vapour Deposition Growth of Few-Layer Hexagonal Boron Nitride. *CrystEngComm* **2017**, *19*, 285–294.
- (14) Roy, T.; Tosun, M.; Kang, J. S.; Sachid, A. B.; Desai, S. B.; Hettick, M.; Hu, C. C.; Javey, A. Field-Effect Transistors Built from All Two-Dimensional Material Components. *ACS Nano* **2014**, *8*, 6259–6264.
- (15) Akinwande, D.; Petrone, N.; Hone, J. Two-Dimensional Flexible Nanoelectronics. *Nat. Commun.* **2014**, *5*, 5678.
- (16) Sheng, Y.; Xu, W.; Wang, X.; He, Z.; Rong, Y.; Warner, J. H. Mixed Multilayered Vertical Heterostructures Utilizing Strained Monolayer WS₂. *Nanoscale* **2016**, *8*, 2639–2647.
- (17) Li, M. Y.; Chen, C. H.; Shi, Y.; Li, L. J. Heterostructures Based on Two-Dimensional Layered Materials and Their Potential Applications. *Mater. Today* **2016**, *19*, 322–335.
- (18) Expanding Our 2D Vision. *Nat. Rev. Mater.* **2016**, *1*, 16089.

- (19) Lee, G. H.; Yu, Y. J.; Cui, X.; Petrone, N.; Lee, C. H.; Choi, M. S.; Lee, D. Y.; Lee, C.; Yoo, W. J.; Watanabe, K.; Taniguchi, T.; Nuckolls, C.; Kim, P.; Hone, J. Flexible and Transparent MoS₂ Field-Effect Transistors on Hexagonal Boron Nitride-Graphene Heterostructures. *ACS Nano* **2013**, *7*, 7931–7936.
- (20) Bonaccorso, F.; Sun, Z.; Hasan, T.; Ferrari, A. C. Graphene Photonics and Optoelectronics. *Nat. Photonics* **2010**, *4*, 611–622.
- (21) Zhang, H. Ultrathin Two-Dimensional Nanomaterials. *ACS Nano* **2015**, *9*, 9451–9469.
- (22) Zhang, X.; Shao, Z.; Zhang, X.; He, Y.; Jie, J. Surface Charge Transfer Doping of Low-Dimensional Nanostructures toward High-Performance Nanodevices. *Adv. Mater.* **2016**, *28*, 10409–10442.
- (23) Wang, W.; Niu, X.; Qian, H.; Guan, L.; Zhao, M.; Ding, X.; Zhang, S.; Wang, Y.; Sha, J. Surface Charge Transfer Doping of Monolayer Molybdenum Disulfide by Black Phosphorus Quantum Dots. *Nanotechnology* **2016**, *27*, 505204.
- (24) Xiang, D.; Han, C.; Wu, J.; Zhong, S.; Liu, Y.; Lin, J.; Zhang, X.-A.; Ping Hu, W.; Özyilmaz, B.; Neto, A. H. C.; Wee, A. T. S.; Chen, W. Surface Transfer Doping Induced Effective Modulation on Ambipolar Characteristics of Few-Layer Black Phosphorus. *Nat. Commun.* **2015**, *6*, 6485.
- (25) Tan, H.; Fan, Y.; Zhou, Y.; Chen, Q.; Xu, W.; Warner, J. H. Ultrathin 2D Photodetectors Utilizing Chemical Vapor Deposition Grown WS₂ with Graphene Electrodes. *ACS Nano* **2016**, *10*, 7866–7873.
- (26) Johari, P.; Shenoy, V. B. Tuning the Electronic Properties of Semiconducting Transition Metal Dichalcogenides by Applying Mechanical Strains. *ACS Nano* **2012**, *6*, 5449–5456.
- (27) Wang, Y.; Cong, C.; Yang, W.; Shang, J.; Peimyoo, N.; Chen, Y.; Kang, J.; Wang, J.; Huang, W.; Yu, T. Strain-Induced Direct-Indirect Bandgap Transition and Phonon Modulation in Monolayer WS₂. *Nano Res.* **2015**, *8*, 2562–2572.

- (28) He, Y.; Yang, Y.; Zhang, Z.; Gong, Y.; Zhou, W.; Hu, Z.; Ye, G.; Zhang, X.; Bianco, E.; Lei, S.; Jin, Z.; Zou, X.; Yang, Y.; Zhang, Y.; Xie, E.; Lou, J.; Yakobson, B. I.; Vajtai, R.; Li, B.; Ajayan, P. M. Strain Induced Electronic Structure Changes in Stacked van Der Waals Heterostructures. *Nano Lett.* **2016**, *16*, 3314–3320.
- (29) Conley, H. J.; Wang, B.; Ziegler, J. I.; Haglund, R. F.; Pantelides, S. T.; Bolotin, K. I. Bandgap Engineering of Strained Monolayer and Bilayer MoS₂. *Nano Lett.* **2013**, *13*, 3626–3630.
- (30) Bao, W.; Jing, L.; Velasco, J.; Lee, Y.; Liu, G.; Tran, D.; Standley, B.; Aykol, M.; Cronin, S. B.; Smirnov, D.; Koshino, M.; McCann, E.; Bockrath, M.; Lau, C. N. Stacking-Dependent Band Gap and Quantum Transport in Trilayer Graphene. *Nat. Phys.* **2011**, *7*, 948–952.
- (31) Kumar, H.; Dong, L.; Shenoy, V. B. Limits of Coherency and Strain Transfer in Flexible 2D van Der Waals Heterostructures: Formation of Strain Solitons and Interlayer Debonding. *Sci. Rep.* **2016**, *6*, 21516.
- (32) Fang, H.; Battaglia, C.; Carraro, C.; Nemsak, S.; Ozdol, B.; Kang, J. S.; Bechtel, H. A.; Desai, S. B.; Kronast, F.; Unal, A. A.; Conti, G.; Conlon, C.; Palsson, G. K.; Martin, M. C.; Minor, A. M.; Fadley, C. S.; Yablonovitch, E.; Maboudian, R.; Javey, A. Strong Interlayer Coupling in van Der Waals Heterostructures Built from Single-Layer Chalcogenides. *Proc. Natl. Acad. Sci.* **2014**, *111*, 6198–6202.
- (33) Marom, N.; Bernstein, J.; Garel, J.; Tkatchenko, A.; Joselevich, E.; Kronik, L.; Hod, O. Stacking and Registry Effects in Layered Materials: The Case of Hexagonal Boron Nitride. *Phys. Rev. Lett.* **2010**, *105*, 046801.
- (34) Li, S.; Li, Q.; Carpick, R. W.; Gumbsch, P.; Liu, X. Z.; Ding, X.; Sun, J.; Li, J. The Evolving Quality of Frictional Contact with Graphene. *Nat. Publ. Gr.* **2016**, *539*, 541–546.
- (35) Lee, C.; Li, Q.; Kalb, W.; Liu, X.-Z.; Berger, H.; Carpick, R. W.; Hone, J. Frictional Characteristics of Atomically Thin Sheets. *Science* **2010**, *328*, 76–80.
- (36) Liu, Z.; Amani, M.; Najmaei, S.; Xu, Q.; Zou, X.; Zhou, W.; Yu, T.; Qiu, C.; Birdwell, A. G.;

- Crowne, F. J.; Vajtai, R.; Yakobson, B. I.; Xia, Z.; Dubey, M.; Ajayan, P. M.; Lou, J. Strain and Structure Heterogeneity in MoS₂ Atomic Layers Grown by Chemical Vapour Deposition. *Nat. Commun.* **2014**, *5*, 5246.
- (37) Dupont. SYNFLEX Quality Network: Teonex Q51. **2015**, 1–3.
- (38) Kim, H. Materials and Design Strategies for Flexible Electronics. Ph.D. Thesis, University of Illinois, Urbana, IL, USA, 2011.
- (39) Zhao, W.; Ghorannevis, Z.; Amara, K. K.; Pang, J. R.; Toh, M.; Zhang, X.; Kloc, C.; Tan, P. H.; Eda, G. Lattice Dynamics in Mono- and Few-Layer Sheets of WS₂ and WSe₂. *Nanoscale* **2013**, *5*, 9677–9683.
- (40) Heller, E. J.; Yang, Y.; Kocia, L.; Chen, W.; Fang, S.; Borunda, M.; Kaxiras, E. Theory of Graphene Raman Scattering. *ACS Nano* **2016**, *10*, 2803–2818.
- (41) Gorbachev, R. V.; Riaz, I.; Nair, R. R.; Jalil, R.; Britnell, L.; Belle, B. D.; Hill, E. W.; Novoselov, K. S.; Watanabe, K.; Taniguchi, T.; Geim, A. K.; Blake, P. Hunting for Monolayer Boron Nitride: Optical and Raman Signatures. *Small* **2011**, *7*, 465–468.
- (42) McCreary, A.; Ghosh, R.; Amani, M.; Wang, J.; Duerloo, K. A. N.; Sharma, A.; Jarvis, K.; Reed, E. J.; Dongare, A. M.; Banerjee, S. K.; Terrones, M.; Namburu, R. R.; Dubey, M. Effects of Uniaxial and Biaxial Strain on Few-Layered Terrace Structures of MoS₂ Grown by Vapor Transport. *ACS Nano* **2016**, *10*, 3186–3197.
- (43) Wang, X.; Jones, A. M.; Seyler, K. L.; Tran, V.; Jia, Y.; Zhao, H.; Wang, H.; Yang, L.; Xu, X.; Xia, F. Highly Anisotropic and Robust Excitons in Monolayer Black Phosphorus. *Nat. Nanotechnol.* **2015**, *10*, 517–521.
- (44) Mohiuddin, T. M. G.; Lombardo, A.; Nair, R. R.; Bonetti, A.; Savini, G.; Jalil, R.; Bonini, N.; Basko, D. M.; Galiotis, C.; Marzari, N.; Novoselov, K. S.; Geim, A. K.; Ferrari, A. C. Uniaxial Strain in Graphene by Raman Spectroscopy: G Peak Splitting, Grüneisen Parameters, and Sample Orientation. *Phys. Rev. B - Condens. Matter Mater. Phys.* **2009**, *79*, 205433.

- (45) Matthewson, M. J.; Kurkjian, C. R.; Gulati, S. T. Strength Measurement of Optical Fibers by Bending. *J. Am. Ceram. Soc.* **1986**, *69*, 815–821.
- (46) Castellanos-Gomez, A.; Barkelid, M.; Goossens, A. M.; Calado, V. E.; Van Der Zant, H. S. J.; Steele, G. A. Laser-Thinning of MoS₂: On Demand Generation of a Single-Layer Semiconductor. *Nano Lett.* **2012**, *12*, 3187–3192.
- (47) Najmaei, S.; Liu, Z.; Ajayan, P. M.; Lou, J. Thermal Effects on the Characteristic Raman Spectrum of Molybdenum Disulfide (MoS₂) of Varying Thicknesses. *Appl. Phys. Lett.* **2012**, *100*, 013106.
- (48) Mitiglu, A. A.; Plochocka, P.; Jadczyk, J. N.; Escoffier, W.; Rikken, G. L. J. A.; Kulyuk, L.; Maude, D. K. Optical Manipulation of the Exciton Charge State in Single-Layer Tungsten Disulfide. *Phys. Rev. B - Condens. Matter Mater. Phys.* **2013**, *88*, 245403.
- (49) Giusca, C. E.; Rungger, I.; Panchal, V.; Melios, C.; Lin, Z.; Lin, Y. C.; Kahn, E.; El??as, A. L.; Robinson, J. A.; Terrones, M.; Kazakova, O. Excitonic Effects in Tungsten Disulfide Monolayers on Two-Layer Graphene. *ACS Nano* **2016**, *10*, 7840–7846.
- (50) Mak, K. F.; He, K.; Lee, C.; Lee, G. H.; Hone, J.; Heinz, T. F.; Shan, J. Tightly Bound Trions in Monolayer MoS₂. *Nat. Mater.* **2013**, *12*, 207–211.
- (51) Trolle, M. L.; Pedersen, T. G.; V?niard, V. Model Dielectric Function for 2D Semiconductors Including Substrate Screening. *Sci. Rep.* **2017**, *7*, 39844.
- (52) He, K.; Poole, C.; Mak, K. F.; Shan, J. Experimental Demonstration of Continuous Electronic Structure Tuning via Strain in Atomically Thin MoS₂. *Nano Lett.* **2013**, *13*, 2931–2936.
- (53) Tsai, M.-Y.; Tarasov, A.; Hesabi, Z. R.; Taghinejad, H.; Campbell, P. M.; Joiner, C. A.; Adibi, A.; Vogel, E. M. Flexible MoS₂ Field-Effect Transistors for Gate-Tunable Piezoresistive Strain Sensors. *ACS Appl. Mater. Interfaces* **2015**, *7*, 12850–12855.
- (54) Harada, N.; Sato, S.; Yokoyama, N. Computational Study on Electrical Properties of Transition Metal Dichalcogenide Field-Effect Transistors with Strained Channel. *J. Appl.*

- Phys.* **2014**, *115*, 034505.
- (55) Sarwat, S. G.; Tweedie, M.; Porter, B. F.; Zhou, Y.; Sheng, Y.; Mol, J.; Warner, J.; Bhaskaran, H. Revealing Strain-Induced Effects in Ultrathin Heterostructures at the Nanoscale. *Nano Lett.* **2018**, *18*, 2467–2474.
 - (56) Susarla, S.; Manimunda, P.; Morais Jaques, Y.; Hachtel, J. A.; Idrobo, J. C.; Syed Amnulla, S. A.; Galvão, D. S.; Tiwary, C. S.; Ajayan, P. M. Deformation Mechanisms of Vertically Stacked WS₂/MoS₂ Heterostructures: The Role of Interfaces. *ACS Nano* **2018**, *12*, 4036–4044.
 - (57) Steinhoff, A.; Kim, J. H.; Jahnke, F.; Rösner, M.; Kim, D. S.; Lee, C.; Han, G. H.; Jeong, M. S.; Wehling, T. O.; Gies, C. Efficient Excitonic Photoluminescence in Direct and Indirect Band Gap Monolayer MoS₂. *Nano Lett.* **2015**, *15*, 6841–6847.
 - (58) Su, L.; Yu, Y.; Cao, L.; Zhang, Y. Effects of Substrate Type and Material-Substrate Bonding on High-Temperature Behavior of Monolayer WS₂. *Nano Res.* **2015**, *8*, 2686–2697.
 - (59) Rivera, P.; Schaibley, J. R.; Jones, A. M.; Ross, J. S.; Wu, S.; Aivazian, G.; Klement, P.; Seyler, K.; Clark, G.; Ghimire, N. J.; Yan, J.; Mandrus, D. G.; Yao, W.; Xu, X. Observation of Long-Lived Interlayer Excitons in Monolayer MoSe₂–WSe₂ Heterostructures. *Nat. Commun.* **2015**, *6*, 6242.
 - (60) Tan, Y.; Ma, L.; Gao, Z.; Chen, M.; Chen, F. Two-Dimensional Heterostructure as a Platform for Surface-Enhanced Raman Scattering. *Nano Lett.* **2017**, *17*, 2621–2626.
 - (61) Rong, Y.; Fan, Y.; Leen Koh, A.; Robertson, A. W.; He, K.; Wang, S.; Tan, H.; Sinclair, R.; Warner, J. H. Controlling Sulphur Precursor Addition for Large Single Crystal Domains of WS₂. *Nanoscale* **2014**, *6*, 12096–12103.

TOC Graphic

